RESEARCH ARTICLE

Dynamical characteristics of the tip vortex from a four-bladed rotor in hover

Swathi M. Mula · James H. Stephenson ·
Charles E. Tinney · Jayant Sirohi

Abstract Dynamical characteristics of tip vortices shed from a 1 m diameter, four-bladed rotor in hover are investigated using various aperiodicity correction techniques. Data are acquired by way of stereo-particle image velocimetry and comprises measurements up to 260° vortex age with 10° offsets. The nominal operating condition of the rotor corresponds to $Re_c = 248{,}000$ and $M = 0.23$ at the blade tip. With the collective pitch set to 7.2° and a rotor solidity of 0.147, blade loading (C_T/σ) is estimated from blade element momentum theory to be 0.042. The findings reveal a noticeable, anisotropic, aperiodic vortex wandering pattern over all vortex ages measured. These findings are in agreement with recent observations of a full-scale, four-bladed rotor in hover operating under realistic blade loading. The principal axis of wander is found to align itself perpendicular to the slipstream boundary. Likewise, tip vortices trailing from different blades show a wandering motion that is in phase instantaneously with respect to one another, in every direction and at every wake age in the measurement envelope.

List of symbols

b	Number of blades
c	Blade chord
C_T	Coefficient of thrust
d_r	Pixel dimension
d_s	Diffraction limited spot diameter
H_ψ	Normalized-helicity
l	Turbulent length scale
L_m	Measurement resolution
M	Blade tip Mach number
Q	Q method
r_c	Vortex core radius
R	Blade radius
Re_c	Blade tip Reynolds number based on chord
T	Rotor thrust
$\mathbf{u} = u, v, w$	Velocity vector with components in y, r, ϕ
u_l	Turbulent velocity scale
V_{tip}	Blade tip velocity
V_θ	Swirl velocity
$V_{\theta,m}$	Peak swirl velocity
y, r, ϕ	Fixed frame coordinates
y', r'	Vortex frame coordinates
$y^\star, r^\star$	Coordinates with respect to mean vortex center
α	Wander orientation with respect to slipstream slope
β	Helix pitch angle
Γ_1	Γ_1 method
ε	Rate of energy dissipation
θ_{1deg}	Blade twist
Λ	Symmetric part of velocity gradient tensor
λ_2	λ_2 method
∇	Gradient operator
ν	Kinematic viscosity
Π	Skew-symmetric part of velocity gradient tensor
ρ_f	Fluid density
ρ_p	Particle density
σ	Rotor solidity
σ_i	Standard of deviation of wander in i direction

S. M. Mula (✉) · J. H. Stephenson · C. E. Tinney · J. Sirohi
Aerospace Engineering and Engineering Mechanics Department,
The University of Texas at Austin, 1 University Station,
C0600, Austin, Texas 78712, USA
e-mail: swathilfjc@gmail.com; cetinney@mail.utexas.edu

🌀 Springer

σ_y	Standard of deviation of axial wander
σ_r	Standard of deviation of radial wander
τ	Kolmogorov time scale
ψ	Wake age in angular coordinates
ψ_v	Vortex age in angular coordinates
Ω	Rotor speed
ω_ψ	ψ component of vorticity vector

1 Introduction

Wandering motions of the blade tip vortex, subsequent to its detachment from the blade surface, add formidable complexity to the shape and behavior of a rotor's wake. In the classical sense, vortex wandering is defined as the random displacement of the vortex core (Gursul and Xie 1999; Ramasamy et al. 2009) and is believed to be driven by inflow unsteadiness, shear layer turbulence, cooperative instabilities (e.g., Crow instability), or the propagation of unsteadiness from the vehicle (Jacquin et al. 2001). This wandering motion smears the statistical properties of the tip vortex, thus making the growth, structure, turbulence, merging, and break-down of these tip vortices difficult to predict over a broad range of operating conditions (Baker et al. 1974; Devenport et al. 1996; Heyes et al. 2004; Bailey and Tavoularis 2008). A persistent difficulty to accurately characterize these blade tip vortices is that it requires whole field measurements. Time averaged single-point measurements using constant temperature anemometers (Iversen et al. 1978; Tung et al. 1981; Green and Acosta 1991) or laser Doppler velocimetry (LDV) instruments (Thompson et al. 1988; Leishman et al. 1996; Han et al. 1997; Bhagwat and Leishman 2000) are corrupted by vortex wandering, thus causing such measurements to be weighted averages in both space and time. For example, increases in the diameter of the vortex core accompanied by reductions in the peak tangential and axial velocities are attributed to wandering, which contributes to apparently high levels of Reynolds stresses (Baker et al. 1974; Devenport et al. 1996; Heyes et al. 2004; Bailey and Tavoularis 2008). Likewise, a premature breakdown of the vortex is likely due to the susceptibility of the vortex to intrusive probes (Green and Acosta 1991). This of course limits reliable measurement techniques to laser-based systems (LDV), which possess restrictions of their own, given the random arrival of particles through the measurement volume and the corrections that must be applied thereafter. While numerous studies have aimed to explore the aperiodicity, vortex wandering and turbulence characteristics of vortices using point techniques (Bhagwat and Leishman 2000; Green and Acosta 1991; Gursul and Xie 1999; Leishman 1998), they fall short of accurately capturing the

true dynamical characteristics of the tip vortex, especially in the far-wake regions where wandering is excessive. This is certainly no fault of the experimentalist, and so has prompted a demand for spatially resolved measurement tools, which have become more sophisticated over the past decade with the advent of commercially available digital particle image velocimetry (PIV) systems.

A unique feature of PIV is the instantaneous measurement of an entire area, providing the velocity distribution in a first post-processing step and allowing for estimates of vorticity, Q, λ_2, etc. in further post-processing. The trade-off, however, is tuned to the challenge of adequately seeding the core of the blade tip vortex. Centrifugal forces cause heavier particles to move outward from the vortex center, thereby resulting in lower levels of scattered light by remaining lighter weight particles residing close to the center. This has prompted several undertakings aimed at improving estimates for the vectors in the vortex core (Ramasamy et al. 2011; Bhagwat and Ramasamy 2012).

In the current study, the trajectory and statistical characteristics of the tip vortices from a four-bladed rotor during hover are captured up to 260° vortex age by way of stereo-PIV and then analyzed using several well-established vortex methods. This is done in an effort to understand the evolutionary characteristics of vortex wander, which continues to be an outstanding question of practical scientific interest (Baker et al. 1974; Devenport et al. 1996; Jacquin et al. 2001; Leishman 1998). The development and subsequent comparison between various vortex aperiodicity correction techniques are certainly not new, and the interested reader should review the work of McAlister (2003), van der Wall and Richard (2006), Ramasamy et al. (2009), Kindler et al. (2010), and Bhagwat and Ramasamy (2012). Here, we employ an arsenal of methods simply to provide confidence in our measurements; the principal focus of this study is on the dynamical characteristics of these blade tip vortices over extended vortex ages, which has received very little attention aside from the work of Kindler et al. (2010).

The outline of this manuscript is as follows. Details of the rotor test stand and instrumentation are discussed in Sect. 2 including an effort to quantify sources of experimental error. The basic statistical properties of the rotor wake are displayed in order to develop an intuition for this complex, three-dimensional flow. Central to this study is the implementation of several different vortex-tracking schemes in Sect. 3, which comprise both divergence and integral-based methods, as well as methods derived from the geometrical properties of the vortex itself. Upon implementation of these vortex-tracking schemes, the slipstream boundary, the dynamics of vortex wander and the rotor slipstream are discussed in Sect. 4, followed by an overall summary of the findings in Sect. 5.

2 Experimental arrangement

2.1 Facility and instrumentation

The current study was conducted at the J.J. Pickle Research Campus of the University of Texas at Austin in a room measuring $6.5 \times 8.0 \times 6.5$ rotor diameters. A custom fabricated rotor test stand provided the necessary conditions for characterizing the vortex trajectory from a four-bladed rotor at various vortex ages. At the heart of this test stand is a 9 kW electric motor capable of producing a maximum rotational speed of 8,000 RPM (133 Hz) and a maximum torque of 10 Nm. Two optical encoders are fixed to the motor and allow both 1/rev and 60/rev positioning of the rotor to be phase aligned with flow measurement instruments.

As for the rotor assembly, a fully articulated, four-bladed hub assembly with flap hinge was mounted on the rotor shaft at a height of three rotor diameters above the ground. The rotor was driven directly by the electric motor, without a transmission. All four rotor blades comprised carbon fiber NACA 0012 profiles with constant chord lengths of 58.5 mm and no twist. Each blade had square tips and a small (<0.8 mm) blunt trailing edge. The diameter of the entire assembly including blades, rotor hub and blade grips was measured to be 1,010 mm; this resulted in a rotor solidity of 0.147.

A collective pitch angle of 7.2° was investigated at a rotor speed of $\Omega = 1,520$ RPM (25.33 Hz) which resulted in a blade tip speed of 80.33 m/s. This corresponded to $Re_c = 248,000$ and $M = 0.23$ at the blade tip. Blade loading was estimated using blade element momentum theory (BEMT): $C_T = 0.0062$, $T = 39.412$ N and $C_T/\sigma = 0.042$, which compares favorably to an integration of the momentum in the rotors wake (Mula et al. 2011). In order to accurately track the rotor blade, lead-lag positions of the blades were fixed (rigid) and adjusted until the blades were visually aligned using a 4/rev strobe. One blade was slightly set behind others, within 5 % of the blade chord, to enforce vortex tumbling as part of a separate study (Stephenson et al. 2012). Often, the unsteady aerodynamic environment in which the blade is moving through causes blade flapping (Richard et al. 2006). This is especially true for rotors operating in ground effect or in small facilities where recirculation patterns cause the rotor disk to re-ingest the unsteady wake. The effect was inspected using the 1/rev strobe and a high resolution digital camera, and revealed flapping motions in the blade tip on the order of 1–2 mm. Similar findings were observed by Sirohi and Lawson (2012) using a digital image correlation technique of the same rotor blades and test stand.

Measurements of the flow along a 2-D slice through the rotor slipstream (y, r) were performed using a 2-camera,

3-component (stereo) PIV system. The orientation of the PIV system's components relative to the rotor test stand is shown in Fig. 1 as well as the axial (y) and radial coordinates (r) with the origin at the center of the rotor hub; these are the in-plane components in rotor coordinates. The azimuthal direction (ϕ) is determined using the right-hand rule and is therefore positive in the direction of the rotor rotation. Furthermore, ψ and ψ_v refer to wake age and vortex age, respectively, whereby, vortex age is defined as the azimuthal age of the vortex filament relative to the blade from which it trailed, whereas wake age defines the azimuthal age of the rotor wake relative to the starting blade (here we choose to use blade 1) and is confined by one rotor revolution. The rotor coordinate system (y, r) corresponds to a fixed frame with its origin located at the center of the hub and in the plane of the rotor disk.

The PIV system's components include a 135 mJ/pulse Nd-YAG laser and two 2M pixel (1,648 × 1,214 pixel) CCD cameras ($f\# = 2.8$) with 14 bit resolution and 7 Hz (double frame mode) sampling frequency. Both cameras have a pixel dimension (d_r) of 7.4 μm. Tests were conducted by phase aligning the first PIV laser pulse with the quarter-chord of the first blade (along its entire length) using the 1/rev optical switch. This assumes that the measurement plane is normal to the vortex axis at all vortex ages. Certainly a slight inclination of the vortex axis is expected; its effect on subsequent results were found to be negligible. Furthermore, the PIV measurement window encompassed an effective field of view of 167 × 150 mm. A total of 36 phase locked positions were studied ($\Delta\psi = 10°$), each comprising 250 statistically independent image pairs at a rate of approximately 4 Hz. And so, at 0°, 90°, 180° and 270° azimuthal positions of
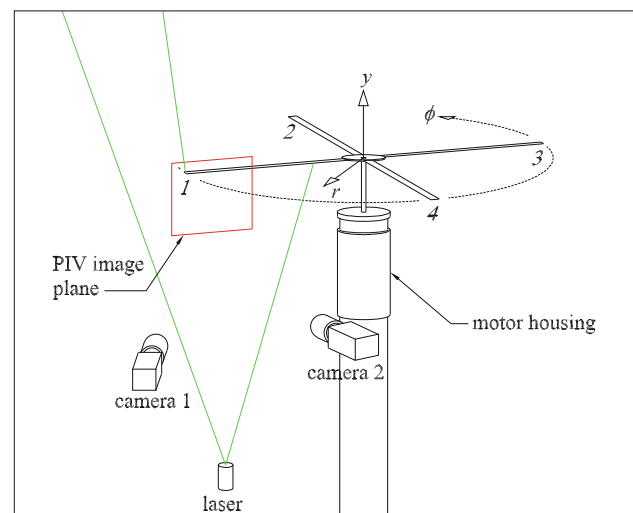
Fig. 1 Orientation of PIV cameras and laser light sheet relative to the rotor test stand with coordinate system

the first blade, the laser sheet was aligned along the quarter-chord of blades 1, 2, 3 and 4, respectively (blade numbers are labeled below each blade tip in Fig. 1). For a sample vortex age of 20°, the maximum azimuthal velocity is on the order of $0.1V_{\text{tip}}$, which falls rapidly to about $0.03V_{\text{tip}}$ at vortex ages greater than 90°. Coupled with an interframe timing rate of 110 μs and a 2 mm laser sheet thickness, these result in a ratio between the laser sheet thickness and the out-of-plane particle displacement of 2.2 and 7.4, respectively. Likewise, the accuracy of the measurement is to within 1° in azimuth based on the rotation speed of the rotor and the interframe timing rate. Seeding was provided by a PIVTEC 14 cascadable Laskin nozzle olive oil seeder with particles ranging between 0.1 and 1 microns in diameter.

Calibration was performed using a plate with known reference points and with calibration parameters being extracted using a pinhole-based model. This was followed by software-based corrections for differences in the viewing angles of the two cameras relative to the image plane. Vector maps were generated using commercial software *DaVis v7.2* from LaVision *GmbH*. Initial interrogation window sizes comprised 32 × 32 pixels that reduced iteratively to a final window size of 16 × 16 pixels thereby resulting in a measurement resolution of $L_m = 2.2$ mm. Based on this setup, L_m/r_c is estimated to be 0.75 (this assumes $r_c = 0.05c$ (van der Wall and Richard 2006)), which is slightly larger than the suggestions of (Grant 1997; Martin et al. 2000) whereby L_m/r_c is expected to be <0.2 for accurate measurements of the core radius r_c. Nevertheless, the focus of the study is on the wandering motion of the vortex, as opposed to the effects of stretching and viscous diffusion; the former of these does not demand conservative values for L_m/r_c. A 50 % overlap was employed and resulted in a spatial grid resolution of 1.0983 mm (0.0187c); a 50 % overlap has been shown to lead to errors for the core radius and peak swirl velocity of up to 5 % (assuming $L_m/r_c < 0.5$) based on Vatistas' model (van der Wall and Richard 2006). The location of the correlation peaks for valid vectors were estimated using a three–point Gaussian fit. Additional details concerning PIV measurement techniques and best practices can be found in Raffel et al. (1998) and the references therein.

2.2 Sources of uncertainty

The principal sources of error in PIV measurements can be categorized into (1) particle tracking, (2) particle imaging and (3) image evaluation. Particle tracking errors are determined for large particle-to-fluid density ratios ($\overline{\rho} = \rho_p/\rho_f \gg 1$) following the analysis of Melling (1997) and Tinney et al. (2008). Given that the rate of energy dissipation (ε) at small scales is equal to the production of energy at large turbulent

scales, ε must be of the order of u_l^3/l, where l and u_l are the integral length and velocity scales of the large scale eddies. Therefore, the time scales of the smallest eddies (Kolmogorov scales) are approximated by $\tau = (\nu\varepsilon)^{1/2}$. The values for l and u_l that are associated with the turbulence in the center of the slipstream are estimated from the mean width and mean convection velocities, respectively, as illustrated in Table 1. Hence, turbulence frequencies never exceed 8.0 kHz, and so, tracking errors for 1.0 μm size particles are found to be within 12 % for the dissipative scales of this flow. Aside from centrifugal forces in the vortex core, the seeding medium chosen for this study reasonably tracks the flow.

A known difficulty with using particle-based techniques to measure blade tip vortices is the lack of seed in the vortex core due to centrifugal forces. A demonstration of this is shown in Fig. 2a using a raw snap-shot at 250° vortex age alongside the resultant vector map in Fig. 2b using vortex frame coordinates. In this snap-shot (and most others), the vortex core comprised approximately 110 vectors. The locations of peak swirl velocities are indicated by the black boundary to provide some reference regarding the size of the vortex core relative to the region of poor light scatter. Likewise, additional lines (horizontal and vertical) have been drawn in Fig. 2b emanating from the vortex center along which the signal to noise ratio (SNR) was recorded and is shown in Fig. 3. SNR is based on the ratio of the primary to secondary correlation peaks in the cross-correlation. For this study, the SNR had to be greater

Table 1 Turbulence frequencies associated with the dissipative scales of the flow at different axial positions below the rotor

y/R	u_l (m/s)	l (mm)	τ^{-1} (kHz)
−0.05	2.26	25	5.43
−0.10	2.98	37	6.75
−0.15	3.13	44	6.67
−0.20	3.25	51	6.55
−0.25	3.68	57	7.47
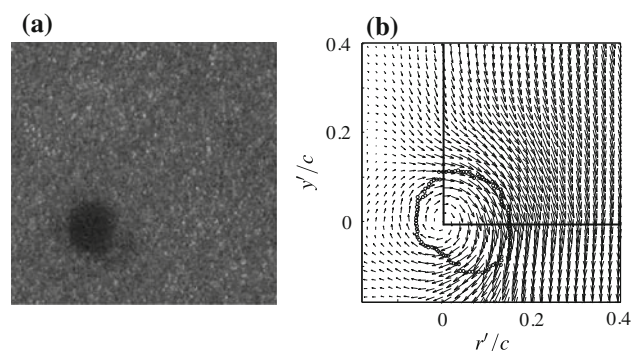
Fig. 2 **a** Raw PIV image at 250° vortex age and **b** its corresponding vector map in PIV coordinates
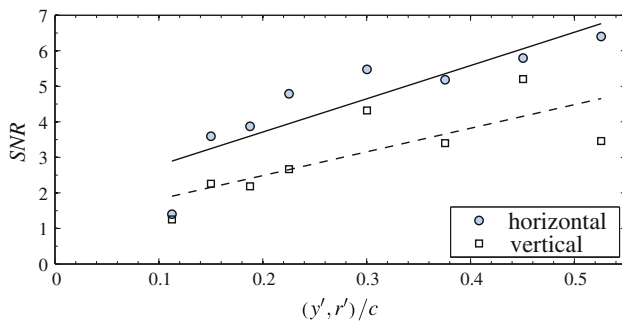
Fig. 3 SNR along the *horizontal and vertical lines* drawn in Fig. 2b

than 1.3 for vectors to be considered valid, after which, missing vectors were estimated using a nearest neighbor fit. The SNR levels in Fig. 3 are shown to be well above the specified threshold and for a large fraction of the vortex.

As for particle imaging errors, the measurement precision depends on the image sensor geometry relative to the particle image diameter (d_s). For a single lens with circular aperture, the diffraction limited spot diameter is well known and relies on an average lens magnification which is found from the calibration to be 0.05. Westerweel (1998) showed that error free estimates can be obtained when $d_s/d_r \geq 2$ where d_r is the pixel size. In the current experiment, d_s/d_r is estimated to be 0.516, which is less than the recommended value of 2. A check for pixel locking effects revealed that the particle image displacements were unbiased by the integer pixel dimension.
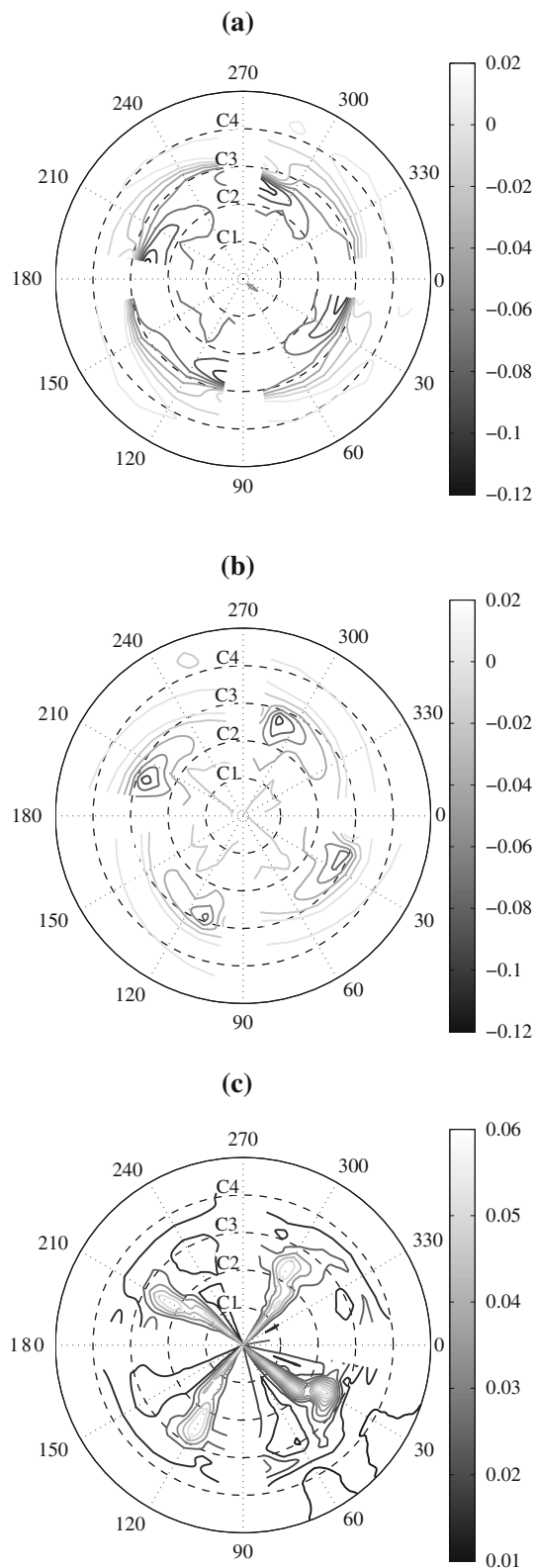
2.3 Rotor wake features

Since the PIV measurements were performed over the entire rotor revolution and along slices in the (y, r) plane, vector maps could be stitched together to view average velocity profiles along slices in the (r, ϕ) plane in order to check for consistency. In Fig. 4a, b, c, contours of the axial, radial and azimuthal velocity components, respectively, of the mean flow are illustrated at an axial position of $y/R = -0.05$ using the raw data without corrections for vortex wander. The center corresponds to the inner most radial position of the PIV measurement window from the rotor hub axis at $r/R = 0.733$. Because of laser blooming effects (laser aligned with quarter-chord of the blade) quality data was unavailable at 0°, 90°, 180° and 270° wake ages. Additional illustrations in Fig. 5 have been included to aid in the discussion of the contours in Fig. 4. These additional illustrations comprise instantaneous slices along the (y, r) plane at 20° and 70° wake ages with a line identifying the plane at $y/R = -0.05$ on which the contours of Fig. 4 are viewed.

Concerning the contour levels in Fig. 4, the mean axial (downwash) and radial (contraction) velocities are of similar levels, as expected, since they collectively display the features associated with vortex swirl. Likewise, as out-of-plane velocities manifest contributions from the maximum axial velocity in the vortex core along with the global swirl velocity (which is small), the out-of-plane velocities are then expected to be smaller than the downwash and contraction velocities, as seen in Fig. 4c.

Upon closer inspection of the contours in Fig. 4, several features describing the trailed and shed wake are observed. Foremost, at this particular y/R position, the principal features in each quadrant are associated with two different vortices. For example, if we consider the first quadrant only (0°–90° wake age) and at 20° wake age, features depicted between C2 and C3 are associated with the top portions of the vortex emitted by blade 4, whereas motions corresponding to the bottom portions of the vortex shed by blade 1 are depicted between C3 and C4 (the same lines corresponding to C1, C2, C3 and C4 have also been drawn in Fig. 5). In Fig. 4a, the axial velocity (depicting motions parallel to the shaft axis) is negative between C2 and C3, thereby indicating downward motions of the inner (high-speed) portion of the vortex (shed from blade 4), whereas it is positive between C3 and C4 to reflect upward motions of the outer (low-speed) portion of the vortex from blade 1. Downward motions are shown to be a factor of six larger in amplitude due to larger convective forces in the higher speed regions of the flow. Likewise, in Fig. 4b, the radial velocity (depicting motions perpendicular to the shaft axis), is negative between C2 and C3 within a 60° wake age to reflect the top portion of the vortex from blade 4 rotating toward the high-speed regions of the slipstream. Between C3 and C4, and nearly 60°–90° wake age, the radial velocity is positive and captures the bottom portion of the vortex from blade 1 as it rotates outward toward the low-speed regions of the flow. As for contours illustrating the azimuthal component of velocity in Fig. 4c, this component is dominant in both the shear layer and vortex core regions of the flow; this is unlike the in-plane components which are only dominant in the vortex core region. The blade wake consistently passes through this y/R position at 30° wake age.

A high degree of similarity is observed between the topographies of each quadrant, which confirms consistency in the flow properties at this axial position. A more rigorous examination at $y/R = -0.05$, -0.10 and -0.15 was performed by Mula et al. (2012) and showed a slight breakdown at distances further away from the rotor plane. More specifically, consistency was found to break first in the radial velocity distribution at $y/R = -0.10$ and then in the axial and out-of-plane components at $y/R = -0.15$. This suggests that there are asymmetries present in the wake of this rotor. Evidence of this will be demonstrated in subsequent discussions pertaining to the slipstream boundary.

(a)

(b)

(c)

◀ **Fig. 4** Contours of the **a** axial (u), **b** radial (v) and **c** azimuthal (w) components of the mean velocity at axial position $y/R = -0.05$. Contour levels are normalized by ΩR. Center corresponds to the radial position: $r/R = 0.733$ with concentric circles (*dashed lines*) C1, C2, C3, C4 corresponding to $r/R = 0.799$, $r/R = 0.865$, $r/R = 0.931$ and $r/R = 0.997$, respectively. The *outer solid line* identifies $r/R = 1.063$, from the rotor hub axis

(a)

(b)
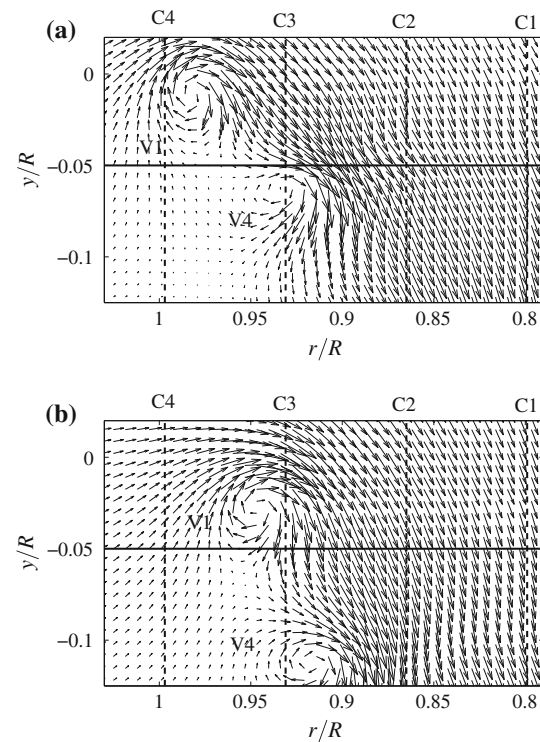
Fig. 5 Average sub-sampled vector map at **a** 20° wake age and **b** 70° wake age. V1 and V4 denote the vortices shed from blades 1 and 4, respectively. The line at $y/R = -0.05$ identifies the plane along which the contours in Fig. 4 are generated

3 Analysis techniques

In an effort to track the location of the vortices from each PIV snap-shot, a method for determining the location of the

vortex center is required. In this regard, a number of schemes have been proposed for identifying vortex cores; for a comprehensive review, see Chakraborty et al. (2005), Cucitore et al. (1999), McAlister (2003) and van der Wall and Richard (2006). Of particular interest are the well-known Q and λ_2 criteria of Hunt et al. (1988) and Jeong and Hussain (1995), respectively. Likewise, centroid of vorticity and normalized-helicity (Levy et al. 1990) have become common metrics for correcting for vortex wander; a comparative study of these various techniques, as they are applied to problems in rotorcraft, can be found in the open literature (Ramasamy et al. 2009).

Because the aforementioned methods are based on divergences of the velocity field, their accuracies in pinpointing the location of the vortex core have been the subject of scrutiny. To this end, Graftieaux et al. (2001) proposed a non-Galilean–invariant method which we will

consider as part of our analysis. This Γ_1-method, however, possesses restrictions that are common to others. In particular, poor seeding levels in the core of the vortex degrade the accuracy of the estimated vectors, thus making corrections for aperiodicity problematic. In this regard, an additional method based on the geometric center of the vortex is employed, which considers only those regions of the vortex where measurements are believed to be accurate. By instituting a conservative level of filtering to the SNRs of the PIV data, only regions in the vortex core residing in close proximity to the peak swirl velocity are considered valid. Corrections for vortex aperiodicity are then determined from an estimate of the geometric center using the peak swirl velocity. In what follows, a brief outline of these techniques is provided followed by a comparison of their results.

3.1 Centroid of Q (CoQ)

The centroid of Q determines the area center of scalar Q as described by van der Wall and Richard (2006). The second invariant, Q, comprises the symmetric (Λ) and skew-symmetric (Π) components of the velocity gradient tensor, defined as,

$$Q = \frac{1}{2}\left(u_{i,i}^2 - u_{i,j}\,u_{j,i}\right) = -\frac{1}{2}\left(u_{i,j}u_{j,i}\right) = \frac{1}{2}\left(\|\Pi\|^2 - \|\Lambda\|^2\right) \tag{1}$$

where $\|\Pi\| = \mathrm{tr}[\Pi\Pi^t]^{1/2}$, $\|\Lambda\| = \mathrm{tr}[\Lambda\Lambda^t]^{1/2}$ and $\Lambda_{ij} = \frac{1}{2}(u_{i,j} + u_{j,i})$, $\Pi_{ij} = \frac{1}{2}(u_{i,j} - u_{j,i})$. Subscripts are written to define the derivative of the first subscript with respect to the second where $i, j = 1, 2, 3$. Thus, the region of vorticity intensity is identified by the region of positive Q. If one wishes to pinpoint a center for the vortex core, then they may choose to consider the centroid of the positive Q region; hence, centroid of Q (van der Wall and Richard 2006). Here the centroid of Q (Y_c, R_c) is determined as,

$$(Y_c, R_c) = \left(\frac{\sum yQ(y,r)}{\sum Q(y,r)}, \frac{\sum rQ(y,r)}{\sum Q(y,r)}\right). \tag{2}$$

This is analogous to the center of mass approach where the numerator on the right-hand side of (2) would represent the sum of mass moments about the respective axis while the denominator would represent the total mass (Mula et al. 2011). For this centroid of Q approach, only those regions with $Q(y,r) > 0$ are considered.

3.2 Centroid of vorticity

The centroid of vorticity is similar to the CoQ method previously described. However, the unavailability of vorticity in all three directions reduces vorticity to the following simplified expression,

$$\omega_\psi = \frac{\partial v}{\partial y} - \frac{\partial u}{\partial r}. \tag{3}$$

The vortex center using this method is identified as the centroid of ω_ψ on 2-D slices (y, r) of the rotor slipstream where measurements are performed.

3.3 Normalized-helicity

Helicity was first introduced by Levy et al. (1990) and is defined as the cosine of the angle between velocity and vorticity and is hence called normalized-helicity. Because of the unavailability of vorticity in all three directions, the expression for normalized-helicity reduces to,

$$H_\psi = \frac{w \cdot \omega_\psi}{|\mathbf{u}||\omega_\psi|}. \tag{4}$$

In the normalized-helicity method, vortex core lines are identified by first locating maximal points of normalized-helicity on cross-sectional planes from which a core line is grown by tracing a streamline through maximal points. Hence, in the current study, vortex centers, using normalized-helicity, are identified as maximal normalized-helicity points on each of the 2D slices through the rotor slipstream. For the CoQ, centroid of vorticity and normalized-helicity techniques, divergences are performed using first-order central differencing.

3.4 Γ_1-Method

The Γ_1-method is a non-Galilean invariant approach introduced by Graftieaux et al. (2001) which provides a simple and robust way to identify centers of vortical structures in a flow. This method defines a scalar function Γ_1 as,
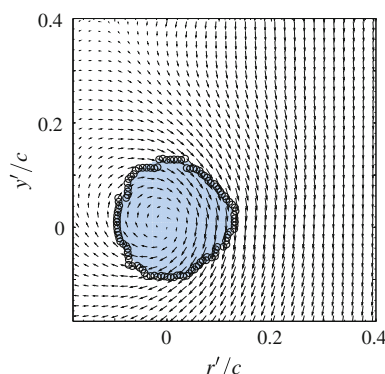
$$\Gamma_1(P) = \frac{1}{N}\sum_S \frac{(PM \times U_M)\cdot \hat{e}_z}{|PM||U_M|}, \tag{5}$$

where PM defines the radius vector between a fixed point P in the measurement domain and all other points M, for a given estimate of $\Gamma_1(P)$. Likewise, S is the region enclosing M, $\hat{e}_z$ is the unit vector normal to the measurement plane and U_M is the total velocity vector at point M. Details of the above expression can be found in Graftieaux et al. (2001) and Kindler et al. (2010). The vortex center is identified by a point where Γ_1 is maximum. Being an integral-based approach, the results are not corrupted by noise introduced by divergences of the velocity field, albeit, the vortex center still relies on an accurate assessment of the velocity inside the vortex core where seeding is poor.
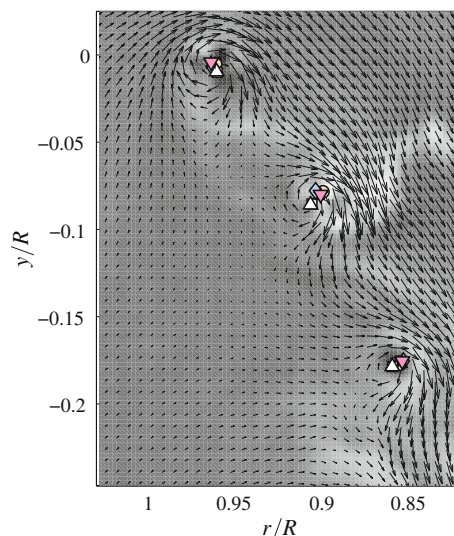
3.5 Geometric center

Once again, poor seeding due to strong centrifugal forces acting inside the vortex core results in the deletion of displacement vectors that fail to meet a satisfactory SNR threshold. Missing vectors are typically interpolated using a nearest neighbor type approach which raises concerns regarding the accuracy of the interpolation. However, Fig. 3 illustrates acceptable SNR levels leading up to, and outside, the peak swirl velocity. Therefore, in the geometric center approach, the center of the vortex core is based on the location of peak swirl velocity and not the velocity inside the core. This provides confidence in the bounds used to define the geometry of the vortex and hence the location of the vortex core. A demonstration of this is shown in Fig. 6 from a raw PIV vector map using lightly shaded regions to identify where $Q > 0$ with dark circles depicting locations of peak swirl velocity. Remarkable similarities in the boundaries of positive Q and the peak swirl velocity are manifest. The geometric center is then identified from the boundaries defined by the peak swirl velocity and is done so using two different approaches. The first of these applies a best fit ellipse to the bounds of the peak swirl velocity whereby the geometric center is identified as the center of this ellipse (referred hereafter as GC-ellipse). In the second approach, the geometric center is identified as the average location of all points confined by the bounds of the peak swirl velocity (referred hereafter as GC-average). We will show later that these two approaches produce indistinguishable results.

The location of the vortex center for each of the three vortices in the measurement window captured by the PIV system are analyzed separately. Figure 7 shows a sub-sampled PIV vector map at 40° wake age with the vortex centers identified using CoQ, maximum-normalized-helicity, centroid-of-vorticity, the Γ_1-method and geometric center (both approaches) to demonstrate the subtle differences among the techniques. All methods are applied to the

Fig. 7 Sub-sampled PIV vector map at 40° wake age. Vortex centers detected using CoQ (*circle*), maximum-normalized-helicity (*square*), centroid-of-vorticity (*diamond*), Γ_1-method (*triangle-up*), GC-ellipse (*star*) and GC-average (*triangle-down*)

250 PIV snap–shots at every wake age from which the position of each vortex is tracked. The results of this are shown in Fig. 8 for a wake age of $\psi = 40°$ using the CoQ approach. Open circles mark the average location of the vortices based on the 250 PIV snap-shots. It can be seen from this illustration how the region of space over which the vortex wanders increases with vortex age. Close inspection reveals how vortex 3 encompasses nearly three times the region of space as vortex 1. Heyes et al. (2004) showed how wandering amplitudes of the tip vortex increase linearly with streamwise distance; similar trends are observed here.
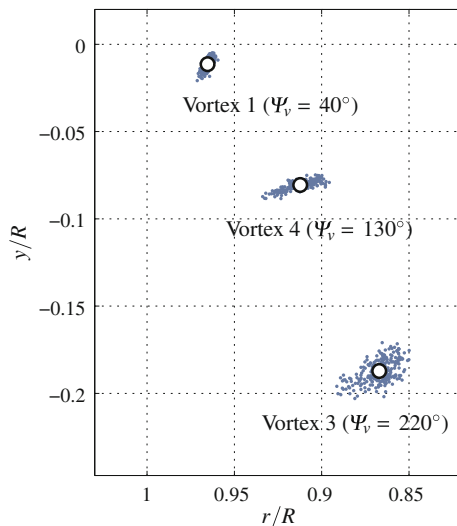
4 Discussion of results

4.1 Slipstream boundary

Based on a systematic series of measurements of a rotor in hover, Landgrebe (1972) showed that the axial and radial coordinate of the tip vortex could be estimated using the following approximate relations:

$$\frac{y}{R} = \begin{cases} k_1 \psi_v; & 0 \leq \psi_v \leq \frac{2\pi}{b} \\ \left(\frac{y}{R}\right)_{\psi_v = \frac{2\pi}{b}} + k_2\left(\psi_v - \frac{2\pi}{b}\right); & \psi_v \geq \frac{2\pi}{b} \end{cases} \quad (6)$$

$$\frac{r}{R} = A + (1-A)e^{-\eta\psi_v} \quad (7)$$

where b is the number of blades, the constant k_1 is the vertical transport velocity of the tip vortex divided by the rotor tip speed and can be uniquely determined from known values of C_T/σ as,

Fig. 6 Q method applied to a sample vortex at 250° vortex age. *Dark circles* identify locations of peak swirl velocity

Fig. 8 Location of vortex centers at 40° wake age using the CoQ approach. Average centers are identified by *large open circles*

$$k_1 = -0.25(C_T/\sigma + 0.001\theta_{1deg}), \qquad (8)$$

while the constant k_2 is the tangent of the local pitch angle of the contracted helix (β_ψ) of the tip vortex in the stable near-field region described by,

$$k_2 = -(1.41 + 0.0141\theta_{1deg})\sqrt{(C_T/2)}. \qquad (9)$$

Likewise, radial coordinates can be determined by substituting $A = 0.78$ and $\eta = 0.145 + 27C_T$ into Eq. (7). With the blade loading estimated from BEMT and for untwisted blades, $\theta_{1deg} = 0$, the radial and axial displacement measurements from the PIV surveys are compared with the estimate provided by way of Landgrebe's model. The results from this are shown in Fig. 9a with the axial and radial displacements of vortices shedding from blades 2 and 3 agreeing well with Landgrebe (1972). Differences in the displacements of vortices from blades 1 and 4 are manifest and are attributed to the rotor wake asymmetry produced by dissimilarities in blade tracking; tumbling between vortices 1 and 4 are shown to commence at a wake age of 210° (this corresponds to a vortex age of 210° for vortex 1 and a vortex age of 300° for vortex 4). Rotor wake asymmetry is also evident in the vortex trajectories demonstrated in Fig. 9b and are difficult to remove for multibladed rotor studies. Nevertheless, these asymmetries were not found to impact the findings. Proof of this will be demonstrated in subsequent analysis of the dynamical characteristics of vortex wander in hover.

4.2 Dynamics of vortex wander

The principal motivation of this study is to develop an understanding for the dynamical characteristics of the blade
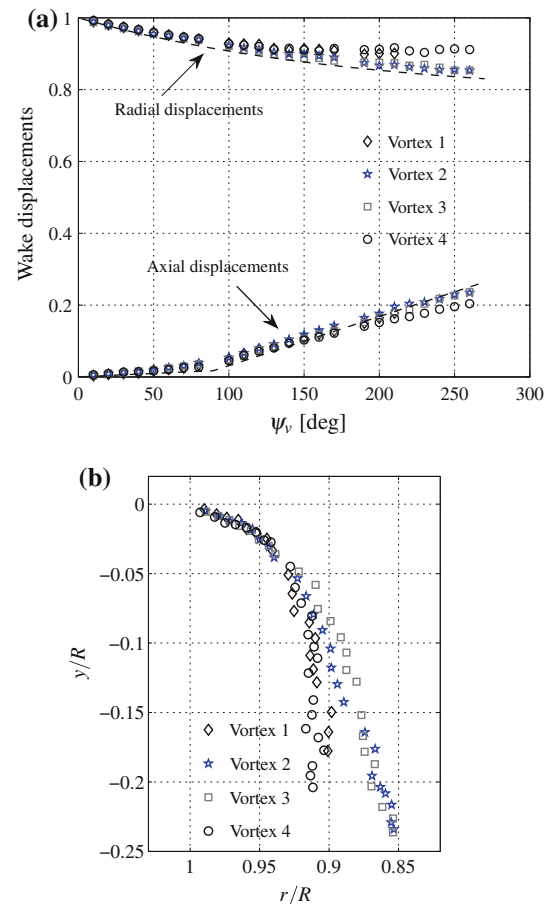
Fig. 9 a Estimates of radial (r/R) and axial (y/R) wake displacements from the current measurements (*diamonds, stars, squares* and *circles*) compared with the predictions from Landgrebe (1972) (*dashed*). The ordinate axis has been normalized by the blade radius. **b** Slipstream boundary from the current measurements

tip vortex motion during hover. Previous studies on the aperiodic characteristics of the tip vortex locations using flow visualization and LDV techniques on one-bladed and two-bladed rotors by Leishman (1998) showed that aperiodic fluctuations of the vortex core position at older wake ages appeared slightly greater in the radial direction than in the axial direction. Recent studies by Kindler et al. (2010) using a stereo-PIV system on a full-scale four-bladed rotor, found that the aperiodicity was not isotropic but was larger in the normal direction than in the spanwise (radial) direction. The findings of Kindler et al. (2010) were confined to a vortex age of 30° but were performed on a full-scale helicopter in hover while operating under realistic blade loading and compressibility effects ($M = 0.64$). Likewise, Beresh et al. (2010) found no Mach number dependence for speeds ranging between Mach 0.5 and 0.8 of a fin trailing vortex (fixed wing study). And so, for the time being, we expect the results from this analysis to be independent of Reynolds number and compressibility effects.
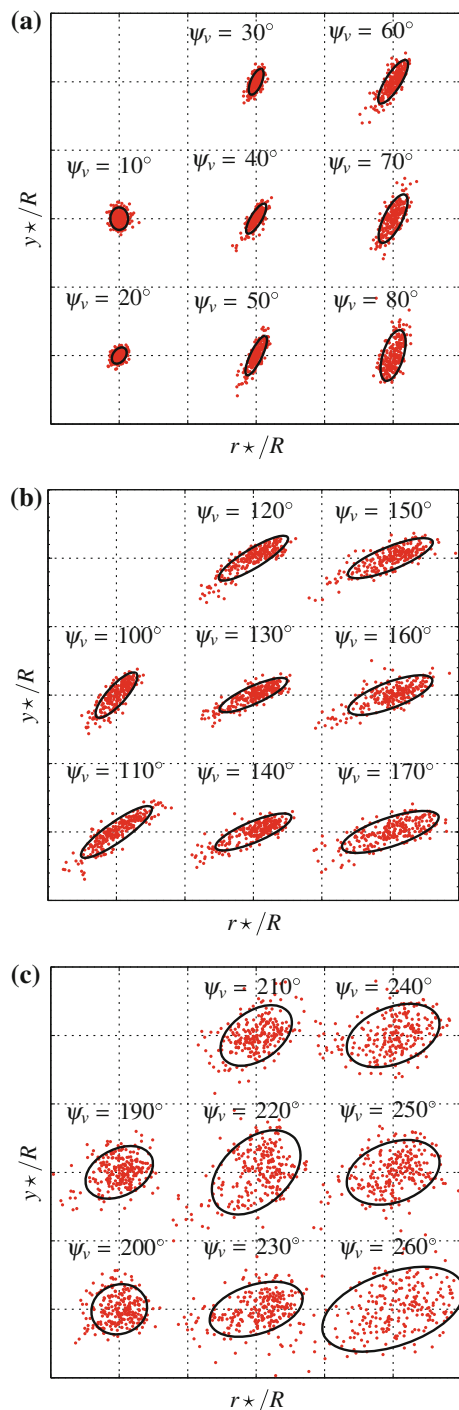
Fig. 10 Wander of vortex from blade 2 overlaid the 95 % confidence region for vortex ages between **a** 10°–80°, **b** 100°–170°, **c** 190°–260° using CoQ. *Dashed lines are separated by* $y^\star/R = 0.03$; $r^\star/R = 0.03$

In Fig. 10, vortex wander, tracked by way of the CoQ approach, is shown for the vortex shed from blade 2 and for vortex ages between 10°–80°, 100°–170° and 190°–260° (similar findings were observed for vortices shed from blades 1, 3 and 4 until vortex tumbling). $(y^\star, r^\star)$ defines

coordinates from the mean vortex center as opposed to the rotor hub. A clear pattern is manifest. At each vortex age, the core has a preferred direction of wander which shows that aperiodic fluctuations in the tip vortex locations are anisotropic. The preferred direction of wander rotates with increasing vortex age and the amount of wander increases with increasing vortex age. The above analysis assumes that the measurement plane was normal to the vortex axis. This assumption was scrutinized by calculating the rotation angles about the radial and axial axes as described by van der Wall and Richard (2006) (required to determine the plane normal to the true vortex axis). The corrections were found to have an indistinguishable effect on the wander pattern. These patterns persist up to a vortex age of $\psi_v = 260°$. Similar observations were found using maximum-normalized-helicity, centroid-of-vorticity, the Γ_1–method and both geometric center approaches; a more comprehensive comparison of these various methods are provided by Mula et al. (2012). These findings support the observations of Kindler et al. (2010), however, we show here that the anisotropic aperiodic motion of the tip vortex persists at all vortex ages in the measurement envelope. The exact mechanisms responsible for inducing the preferred wander direction and wander rotation are not clearly understood. It is postulated that these are the consequence of linear wake instabilities (Widnall 1972; Ohanian et al. 2012) that become excited by perturbations in the blade tip motion.

Figure 11 demonstrates the vortex wander with the 95 % confidence region overlaid the mean slipstream boundary for an arbitrarily chosen vortex (vortex shed from blade 2) using the CoQ method. The illustration shows that the principal wandering axis aligns itself orthogonal to the mean slipstream boundary. In order to determine this more definitively, the angle (α) between the preferred direction of wander and the slope of the slipstream boundary is determined at every vortex age, following the schematic in Fig. 12a. The results of this are shown in Fig. 12b. At any vortex age, the slope of the slipstream boundary can be determined by the direction of the velocity of the vortex at that age. It is evident from Fig. 12b that the direction of wander is predominantly orthogonal to the mean slipstream boundary. Here, we have plotted the results using all methods to demonstrate the insensitivity of this behavior to the analysis technique used. Noticeable deviations from orthogonality at 10° and 80° vortex ages is attributed to the close proximity of the vortex to the outgoing and oncoming blades, respectively, which resulted in inaccurate slope estimates at these vortex ages. Concurrent studies by Karpatne et al. (2012) observed nearly identical results using a vortex ring emitter model. Likewise, the consistency of these findings for all vortices shed from the four blades was shown by
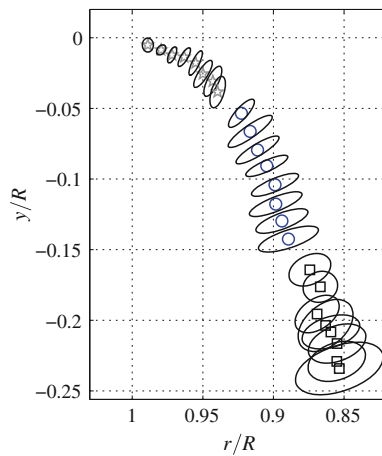
Fig. 11 Mean slipstream boundary (*stars*: $\psi_v = 10°–80°$, *circles*: $\psi_v = 100°–170°$, and *squares*: $\psi_v = 190°–260°$) with the 95 % confidence region at each vortex age using CoQ for the vortex from blade 2
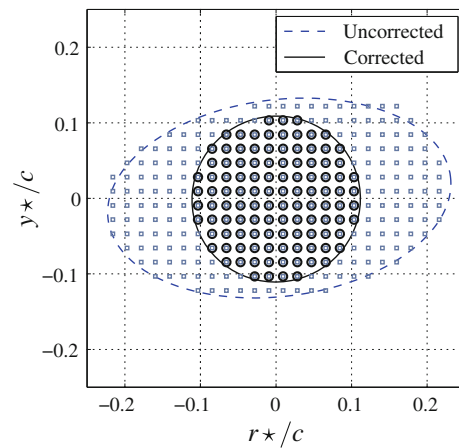
Fig. 13 Boundaries of the vortex core identified by the Q criterion for a vortex at 220° vortex age and fitted to a best possible ellipse (*dashed lines* with *square* data points indicate before aperiodicity correction, while *solid lines* and *circles* are designated for after correction)
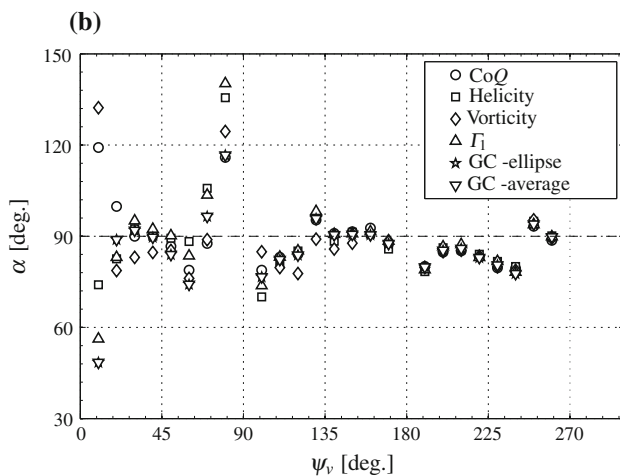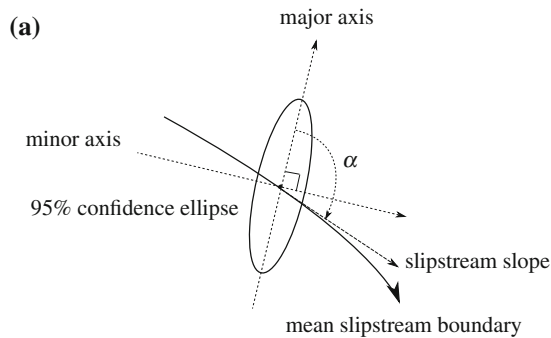
Fig. 12 a Schematic used to describe the orientation of wander with respect to the mean slipstream boundary. **b** Quantitative measure of the wander orientation with respect to the mean slipstream boundary for the vortex from blade 4 using various aperiodicity correction techniques

Mula et al. (2012) and suggests that aperiodic vortex motion occurs irrespective of asymmetries in the slipstream.

The shape of the vortex core at 220° vortex age (arbitrarily chosen) is shown in Fig. 13 with and without corrections for aperiodicity. The boundaries of the corrected and uncorrected vortices are defined using the Q criterion using squares and circles to identify locations where $Q > 0$, respectively. These boundaries are restricted by the resolution of the PIV vector map and so the vortex core is fitted with a best possible ellipse. As expected, the size and shape of the uncorrected vortex is remarkably different than that of the corrected vortex (see Fig. 13) due to wandering.

As for the evolutionary characteristics of the vortex wander, the ratio σ_i/c is plotted in Fig. 14 where σ_i is the standard of deviation of vortex wander and is separated into components acting normal ($i = 1$) and tangential ($i = 2$) to the slipstream boundary. A third order least squares fit, based on the average of all trends produced by the various aperiodicity correction techniques, has been inserted to aid in the interpretation. It is seen here how wandering motions acting normal to the slipstream boundary develop much earlier than the tangential wandering motions. By 180° vortex age, both normal and tangential wandering motions appear to grow at similar rates. By 260°, the normal scatter appears to be at its minimum rate of change, while the tangential scatter is undergoing its maximum rate of change. It is postulated that both will eventually converge toward equal measures of spatial displacement further downstream where the rotor wake no longer contracts, and vortex wander can be assumed isentropic.

4.3 Dynamics of the rotor slipstream

The linear stability of a helical vortex filament to in-plane sinusoidal perturbations (Widnall 1972) revealed three
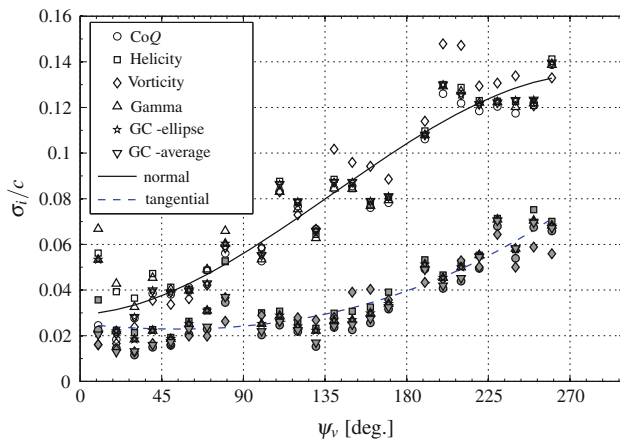
Fig. 14 Average variation in the normal (*open symbols*) and tangential (*closed symbols*) displacements of the vortex relative to the blade chord

Fig. 15 Schematic of vortex wander and coordinate system (for in-plane motions) with respect to the mean slipstream boundary

instability mode shapes: a short-wave mode, a mutual inductance mode and a long-wave instability. And so, it is highly likely that the shape of the slipstream is dynamic; always undergoing rigid-body-like translation, expansion and contraction effects or other wavenumber type motions. If so, then one would expect the relative in-plane motion of the vortices to act as indicators of this phenomenon.

In order to quantify the relative in-plane motion between vortices, the radial and axial locations of the vortex center for each of the vortices in the PIV measurement window are analyzed separately using CoQ. Restrictions on the size of the image plane, required for accurate PIV measurements, limits the analysis to only three vortices at a given near-field position (see Fig. 7). A schematic is shown in Fig. 15 where $(y^\star, r^\star)$ define the coordinates from the mean vortex center. The three vortices depicted in Fig. 15 are labeled vortex 1, 4 and 3 as they form from blades 1, 4 and 3, respectively. Further, displacements are normalized with the standard deviation (σ_y, σ_r) of the corresponding component to eliminate the amplitude dependence brought upon by the spatial growth in the wander motion with increasing vortex age.

Figure 16a, b depict instantaneous displacements in the axial and radial directions, respectively, of vortex 4 with vortex 3 for wake ages between 10° and 80°. Once again, a 95 % confidence region is constructed which identifies a preferred direction of orientation inclined at 45° to the horizontal axis at all wake ages. Similar findings were observed between vortex 1 and 4, and vortex 1 and 3 (Mula et al. 2012). Because these displacements are confined to an analysis between vortices within one quadrant of the slipstream and up to only 260° vortex age, predictions about the dynamics of the rotor slipstream beyond 260° vortex age are purely hypothetical. Hence, from Fig. 16, it
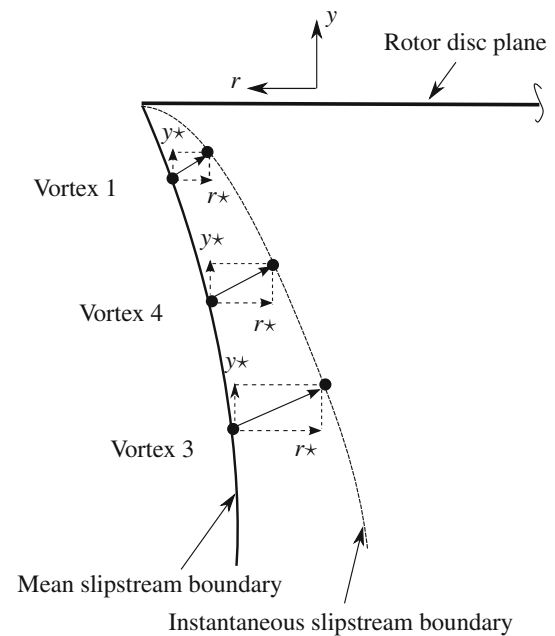
can be deduced that all three vortices in the measurement window wander in phase instantaneously in the radial and axial directions. This finding conveys a number of plausible scenarios concerning the dynamics of the slipstream. The first of these is a semi-rigid-body translation of the slipstream boundary driven by the formation of long-wave instability modes. For this to be the case, non-integer multiples of the mode number could be present so long as the mode number is on the order of tenths; only one zero-crossing per several revolutions of the helix. In other words, non-integer number instabilities (which can form in a helix) will cause in-plane motions of the vortex filament to be spatially out of phase; Fig. 16 shows these motions to be in phase. Likewise, small-wave instabilities comprising mode numbers made up of integer multiples may also be present and for the same reasons just described.

Bhagwat and Leishman (2000) applied linear stability analysis to a free vortex wake model of a rotor in hover to show that the blade tip vortex filament is dominated by two types of instabilities. The first of these instabilities comprise wavenumbers with integer multiples of the number of blades and are found in the near-field region prior to vortex tumbling. The second of these, which they show to have a stronger growth rate than the first, encompasses wavenumbers with half integer multiples of the number of blades and are responsible for vortex tumbling. Hence, the in-phase wander of vortices observed here suggest the dominance of wavenumbers in the measurement envelope comprising integer multiples of the number of blades.
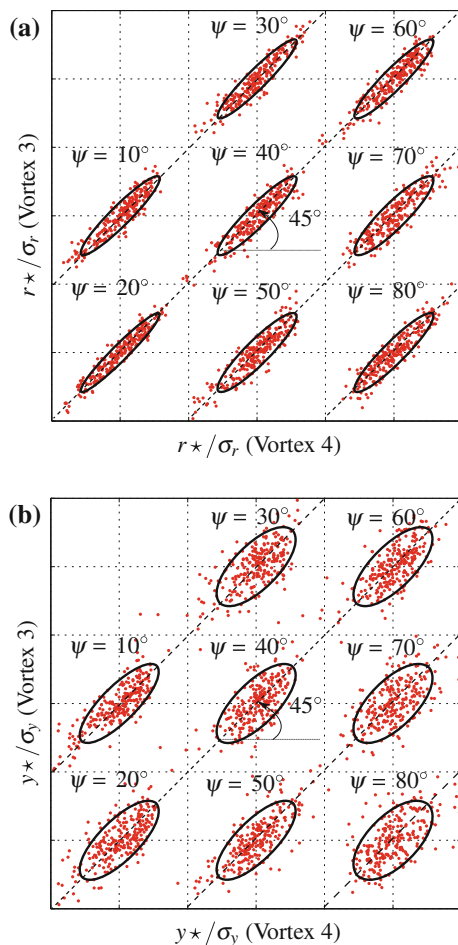
Fig. 16 Phase motion of the **a** radial and **b** axial displacements between vortex 4 and vortex 3, using CoQ. The 95 % confidence interval region has been drawn. *Dashed lines* are separated by $y^\star/\sigma_y = 3$; $r^\star/\sigma_r = 3$

5 Summary

The dynamical and evolutionary characteristics of blade tip vortex wander from a rotor in hover are studied using various aperiodicity correction techniques. This comprises standard vortex methods combined with a centroid of Q (CoQ), centroid of vorticity, normalized-helicity, the Γ_1 integral method and corrections based on geometric center. The last of these eliminates concerns regarding the use of optical-based tools whose measurements are corrupted by poor seeding levels that often occur in the core regions of the vortex. All of the techniques are applied to stereo-PIV measurements up to a vortex age of $\psi_v = 260°$ from a four-bladed rotor in hover with $Re_c = 248{,}000$ and $M = 0.23$ at the blade tip in order to track the trajectory of the blade tip vortex. A 95 % confidence interval of the vortex trajectory reveals a noticeable pattern in the vortex motion with each vortex age comprising a preferred

direction of wander. These aperiodic fluctuations in the tip vortex locations are anisotropic with a preferred direction of wander that rotates with increasing vortex age. The principal axis of the vortex wander motion aligns itself perpendicular to the mean slipstream boundary, while the amount of wander increases with increasing vortex age. The findings persist over the entire vortex age that could be resolved within the restrictions of the PIV measurement window. It is postulated that this aperiodic and anisotropic motion persists until vortex tumbling occurs, or until the rotor wake ceases to contract. The findings are in agreement with the full-scale, four-bladed rotor study of Kindler et al. (2010) under realistic blade loading conditions. Further analysis reveals the in-phase wander of vortices driven by instabilities with wave numbers equal to integer multiples of the number of blades. The initial perturbations are likely driven by deflections in the blade tip. However, it is postulated that the growth of these perturbations with increasing wake age appear to be overcome by linear instabilities within the vortex filament.

References

Bailey SCC, Tavoularis JG (2008) Measurements of the velocity field of a wing-tip vortex, wandering in grid turbulence. J Fluid Mech 601:281–315

Baker GR, Barker SJ, Bofah KK, Saffman PG (1974) Laser anemometer measurements of trailing vortices in water. J Fluid Mech 62:325–336

Beresh SJ, Henfling JF, Spillers RW (2010) Meander of a fin trailing vortex and the origin of its turbulence. Exp Fluids 49:599–611

Bhagwat MJ, Leishman JG (2000) Correlation of helicopter rotor tip vortex measurements. AIAA J 38(2):301–308

Bhagwat MJ, Leishman JG (2000) Stability analysis of helicopter rotor wakes in axial flight. J Am Helic Soc 45(3):165–178

Bhagwat MJ, Ramasamy M (2012) Effect of tip vortex aperiodicity on measurement uncertainty. Exp Fluids 53:1191–1202

Chakraborty P, Balachandar S, Adrian RJ (2005) On the relationships between local vortex identification schemes. J Fluid Mech 535:189–214

Cucitore R, Quadrio M, Baron A (1999) On the effectiveness and limitations of local criteria for the identification of the vortex. Eur J Mech B/Fluids 18(2):261–282

Devenport WJ, Rife MC, Liapis SI, Follin GJ (1996) The structure and development of a wing-tip vortex. J Fluid Mech 312:67–106

Graftieaux L, Michard M, Grosjean N (2001) Combining PIV, POD and Vortex identification algorithms for the study of unsteady turbulent swirling flows. Meas Sci Technol 12(9):1422–1429

Grant I (1997) Particle image velocimetry: A review. Proceedings of the institution of mechanical engineers 211(C):55–76

Green SI, Acosta AJ (1991) Unsteady flow in trailing vortices. J Fluid Mech 227:107–134

Gursul I, Xie A (1999) Origin of vortex wandering over delta wings. J Aircraft 37(2):348–350

Han YO, Leishman JG, Coyne AJ (1997) Measurements of the velocity and turbulence structure of a rotor tip vortex. AIAA J 35(3):477–485

Heyes AL, Jones RF, Smith DAR (2004) Wandering of wing-tip vortex. In: Proc 12th Int Symp Appl Laser Tech Fluid Mech, Lisbon, Portugal

Hunt JCR, Wray AA, Moin P (1988) Eddies, stream, and convergence zones in turbulent flows. Center for Turbulence Research Report: CTR-S88:193–208

Iversen JD, Corsiglia VR, Park S, Backhus DR, Brickman RA (1978) Hot-wire, laser-anemometer, and force measurements of inter-acting trailing vortices. J Aircraft 16(7):448–454

Jacquin L, Fabre D, Geffroy P, Coustols E (2001) The properties of a transport aircraft wake in the extended near field: an experimental study. AIAA Paper 2001–1038

Jeong J, Hussain F (1995) On the identification of a vortex. J Fluid Mech 285:69–94

Karpatne A, Sirohi J, Mula SM, Tinney CE (2012) Investigation of tip vortex aperiodicity in hover. In: American helicopter society 68th annual forum, Fort Worth, USA, May 1–3

Kindler K, Mulleners K, Richard H, van der Wall BG, Raffel M (2010) Aperiodicity in the near field of full-scale rotor blade tip vortices. Exp Fluids 50(6):1601–1610

Landgrebe AJ (1972) The wake geometry of a hovering helicopter rotor and its influence on rotor performance. J Am Helic Soc 17(4):3–15

Leishman JG (1998) Measurements of the aperiodic wake of a hovering rotor. Exp Fluids 25:352–361

Leishman JG, Baker A, Coyne A (1996) Measurements of rotor tip vortices using three-component laser doppler velocimetry. J Am Helic Soc 41(4):342–353

Levy Y, Degani D, Seginer A (1990) Graphical visualization of vortical flows by means of helicity. AIAA J 28(8):1347–1352

Martin PB, Leishman JG, Pugliese GJ, Anderson SL (2000) Stereoscopic PIV measurements in the wake of a hovering rotor. In: American helicopter society 56th annual forum, Virginia, USA, May 2–4

McAlister KW (2003) Rotor wake development during the first revolution. In: American helicopter society 59th annual forum, Phoenix, USA, May 6–8

Melling A (1997) Tracer particles and seeding for particle image velocimetry. Meas Sci Technol 8(12):1406–1416

Mula SM, Stephenson J, Tinney CE, Sirohi J (2011) Vortex jitter in hover. In: American helicopter society southwest region technical specialists meeting, Fort Worth, USA, February 23–25

Mula SM, Stephenson J, Tinney CE, Sirohi J (2012) Dynamical and evolutionary characteristics of the tip vortex from a four-bladed rotor in hover. In: American helicopter society 68th annual forum, Fort Worth, USA, May 1–3

Ohanian CV, McCauley GJ, Savaş O (2012) A visual study of vortex instabilities in the wake of a rotor in hover. J Amer Heli Soc 57(042005):1–8

Raffel M, Willert C, Kompenhans J (1998) Particle image velocimetry - A practical guide. Springer, Berlin

Ramasamy M, Johnson B, Huismann T, Leishman JG (2009) Digital particle image velocimetry measurements of tip vortex characteristics using an improved aperiodicity correction. J Am Helic Soc 54(012004):1–13

Ramasamy M, Paetzel R, Bhagwat WJ (2011) Aperiodicity correction for rotor tip vortex measurements. In: American helicopter society 67th annual forum, Virginia Beach, USA, May 3–5

Richard H, Bosbach J, Henning A, Raffel M, Willert C, van der Wall G (2006) 2C and 3C PIV measurements on a rotor in hover condition. In: Proc 13th Int Symp Appl Laser Tech Fluid Mech, Lisbon, Portugal

Sirohi J, Lawson MS (2012) Measurement of helicopter rotor blade deformation using digital image correlation. J Optical Eng 51(4):43603

Stephenson JH, Mula SM, Tinney CE, Sirohi J (2012) Far wake rotorcraft vortex tumbling. In: 50th AIAA Aerospace sciences meeting and exposition, Nashville, USA, 2012–0425.

Thompson TL, Komerath NM, Gray RB (1988) Visualization and measurement of the tip vortex of a rotor blade in hover. J Aircraft 25(12):1113–1121

Tinney CE, Glauser MN, Ukeiley LS (2008) Low-dimensional characteristics of a transonic jet. Part 1: Proper orthogonal decomposition. J Fluid Mech 612:107–141

Tung C, Pucci SL, Caradonna FX, Morse HA (1981) The structure of trailing vortices generated by model rotor blades. NASA Technical Memorandum 81316

van der Wall BG, Richard R (2006) Analysis methodology for 3C-PIV data of rotary wing vortices. Exp Fluids 40:798–812

Westerweel J (1998) Effect of sensor geometry on the performance of PIV interrogation. In: Proc 9th Int Symp Appl Laser Tech Fluid Mech, Lisbon, Portugal

Widnall SE (1972) The stability of a helical vortex filament. J Fluid Mech 54(4):641–663